



Investigations of Correlation and Coherence in Turbulence from a Large-Eddy Simulation

Regis Thedin, Eliot Quon, Matthew Churchfield, and Paul Veers

National Renewable Energy Laboratory

Correspondence: Regis Thedin (regis.thedin@nrel.gov)

Abstract. Microscale flow descriptions are usually given in terms of statistics of turbulence quantities and/or spectral analysis. Those metrics, while valuable, give limited information about coherent turbulent structures. This work investigates the structure of an atmospheric boundary layer using coherence and correlation in space and time with a range of separation distances. To that end, we obtain spatial correlation of entire planes of velocity fluctuations, which allow us to have a better understanding of the correlation along different directions at different spacings. Similarly, coherence of the three velocity components over separations in the three directions is also investigated. We apply these analyses to a mesoscale-to-microscale coupled scenario with time-varying conditions and examine nuances in spatial correlations that are often overlooked. Through these analyses, we highlight the importance of spatial correlation and coherence for disciplines like wind energy structural dynamic analysis, in which blade loading and fatigue depend strongly on turbulence structure. We emphasize the additional wealth of data that can be provided by typical atmospheric boundary layer large-eddy simulation when correlation and coherence analysis is included, and we also state the limitations of large-eddy simulation data, which inherently truncate the smaller scales of turbulence.

1 Introduction

Offshore deployment of wind farms offers a new set of challenges. As wind turbines increase in rotor diameter, it becomes increasingly important to characterize the flows these large turbines will experience. Knowing how the flow structures evolve over increased geographic extent of wind plants is relevant to turbine and wind plant design. In fact, a better understanding of atmospheric and wind farm flow physics has been identified as one of the grand challenges in wind energy research (Veers et al., 2019), noting the coupling between mesoscale and microscale flows.

Descriptions of the microscale flow, or the turbulent flow of the atmospheric boundary layer, are usually given as statistics of mean and turbulent quantities and/or spectral analyses. Such metrics, while valuable (e.g. see Robertson et al. (2018)), provide limited information about the spatial or temporal structure of turbulent eddies and how they change as background atmospheric conditions and stability change. Space–time correlation and coherence provide the necessary base for understanding the relation between spatial and temporal scales of motion. The correlations quantify how the fluctuations at one location relate to those at a different location, or how fluctuations at a point are related in time. Coherence is similar, but compares the phase relationship of two points in the frequency domain rather than comparing the values in the time domain. Together, these quantities describe important characteristics of turbulent flow structure across spatial and temporal scales.



The turbulence models suggested by the international wind turbine design standards (IEC 61400-1, 2019) to predict mechanical loads contain mathematical descriptions of spatial coherence. These models include exponential-based equations that impose coherence on a flow based on spectral content descriptions. Accurately capturing how coherences vary with different model parameters, such as separation distance, and change with different velocity components can better inform and improve models. The base of these models go back to the original exponential coherence formulation of Davenport (1961), which is a direct function of reduced frequency and an exponential decay. In Davenport's model, the separation distance is only implicitly accounted for in the reduced frequency. The model fails to account for the reduction of coherence at low frequencies and large separation distances. An improvement of Davenport's model by Kaimal et al. (Kaimal et al., 1972; Thresher et al., 1981) accounts for the separation distance. Kaimal's wind spectra model combined with a coherence function eventually became one of the recommended model in the mentioned IEC guidelines (IEC 61400-1, 2019), alongside Mann's spectral turbulence model (Mann, 1994, 1998). The Mann model, based on the Von Karman (1948) model, assumes that an isotropic energy spectrum is distorted by a linearized mean velocity shear.

The use of models suggested by the IEC standards can result in an overestimation of fatigue loads (Holtslag et al., 2016). The same study, however, noted that the primary sources of fatigue loads, the wind shear and turbulence levels, can vary significantly depending on the stability state. While the IEC-suggested models were developed for neutrally stratified flows, such stability is often not the norm for low wind speed scenarios. The effect of stability on loads has also been studied in Sathe and Bierbooms (2007) and Sathe et al. (2013) by the use of Mann's model with Monin-Obukhov length. While turbulence and shear, separately, cause different loads on blades, tower, and rotor, it was noted that the IEC standards are very conservative on the definition of wind shear and turbulence, which results in a significant overestimation of the loads (the authors note up to 96%) when compared to loads obtained when using wind conditions specific to a site of interest.

Understanding how the coherence changes with varying conditions is important. Recent studies have assessed effects of coherence functions on offshore wind turbine loads (Doubrawa et al., 2019; Nybø et al., 2020), as well as on loads of offshore wind turbine frame structure (Li et al., 2021), and their impact has also been noted in other studies (Kelley et al., 2005; Kelley, 2011). Prior work focused on offshore flows, either by showing the coherence levels of such flows alone (Naito, 1983), or establishing comparisons between observed data to Kaimal and Mann spectral models (Cheynet et al., 2017). Often, all three components of the turbulence vector are analyzed, adding to the prior studies that only considered the streamwise component (e.g. Eidsvik (1985); Andersen and Løvseth (2006)). Unfortunately, usually only vertical separation is studied, given limited instruments arranged in a tower. In general, these studies found that coherence levels based on observations at an offshore environment are higher than those computed by the spectral models. Obtaining the field data required to gain a comprehensive picture of the coherence and correlation of the flow can be challenging—especially with lateral coherence. Meteorological masts are typically deployed in isolation or their spacing is much larger than the size of background turbulent structures, such that the fluctuations are decorrelated between the meteorological masts. Alternatively, computational models, especially turbulence-resolving large-eddy simulations (LES), are particularly well-suited for the task because data can be collected anywhere in the flow field at high frequency. Prior work used LES (Berg et al., 2016; Lukassen et al., 2018; Doubrawa et al., 2019; Nybø et al., 2020) to assess coherence in the flow and compare with models, and in general it was found that the stability



affects shear and turbulence levels, which has a direct effect on the coherent structures, something that is not captured by either Mann or Kaimal models.

In this work we employ LES to compute the flow field within the atmospheric boundary layer and use the generated data to investigate the correlations and coherence present in all components of the turbulence and how they vary over time with varying atmospheric conditions. In particular, the microscale simulations are performed with mesoscale forcing so that regional-scale weather variations in the wind speed, direction, shear, as well as surface heat flux are introduced into the microscale domain. The goal is to highlight the additional information that can be obtained with LES, show how it relates to simple models, and note shortcomings that can benefit from further LES studies.

2 Scenario Investigated

The focus of this work is on a 4-hour period in the North Sea off the German coast near the Netherlands at the FINO1 atmospheric measurement platform, see Fig. 1. The wind during the period of interest is predominantly from the Northwest, so from the open sea.

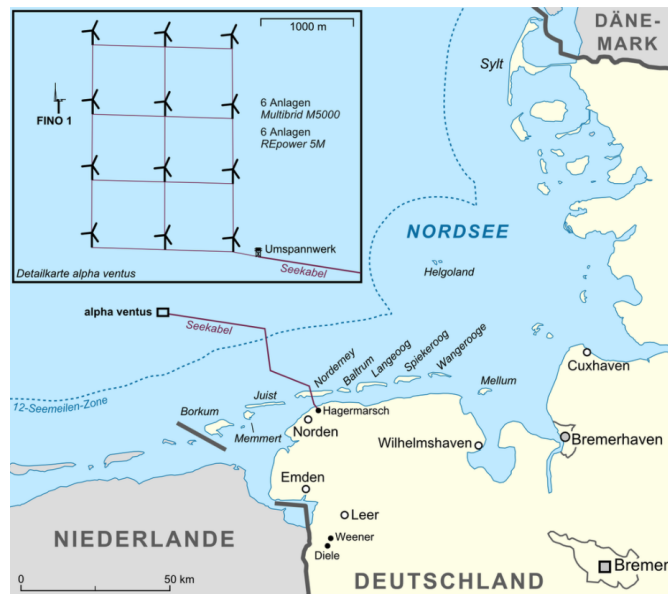


Figure 1. Overview of the region around the Alpha Ventus FINO1 tower. Figure from Wikimedia Commons, distributed under a CC BY-SA 3.0 license.

The period of interest spans from 1 a.m. to 5 a.m. local time on May 16, 2010. The stability state over most of the period is slightly convective. We performed mesoscale-driven LES of the flow in the vicinity of FINO1 during the time period of interest.

The overall background conditions are shown in Fig. 2. While we allow the conditions to change, the period of interest was picked because of the relative small change in wind direction and wind speed. The goal was to have the flow mostly from the



offshore environment, rather than influenced by the nearby land. Turbulence intensity levels of the microscale LES followed well the levels observed in the FINO1 platform. A slight difference in both wind direction and wind speed can be observed. The microscale does not receive any information from the observations, but rather from the mesoscale, which means the microscale will inherit any errors from the mesoscale and will only be as accurate as the mesoscale. The mesoscale coupling provides information on mean profiles, resulting in similar shear histories. Note that turbulence is not resolved at mesoscale resolutions, reflected on Fig. 2(c).

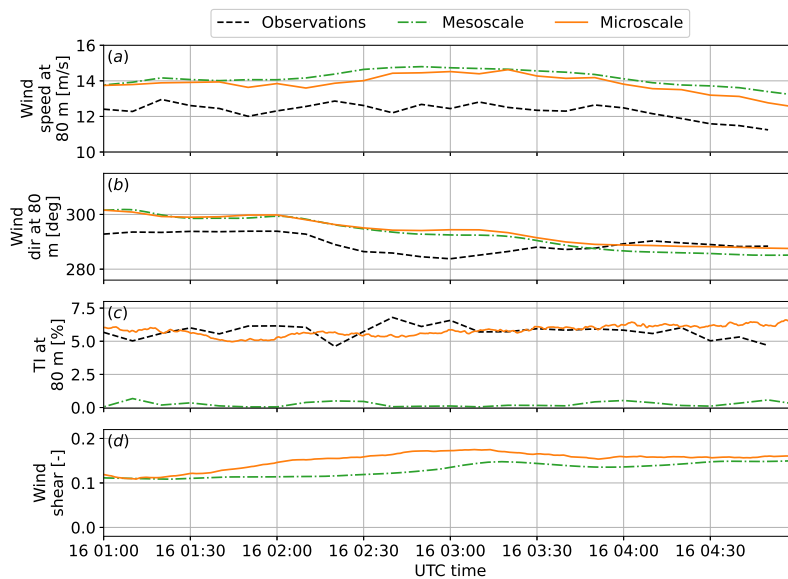


Figure 2. Mean background conditions during the period of interest compared to observation data and the mesoscale solution used to drive the microscale LES.

When applicable, high-frequency sonic anemometer data at the FINO1 tower are compared against the LES data. Sonic anemometer data were available at 40, 60, and 80 m. We picked 80 m as a comparison height and also sampled LES data at that height.

3 Numerical Setup

The simulations are executed using the Simulator for Wind Farm Applications (SOWFA) (Churchfield et al., 2012), an LES code designed for atmospheric and wind-energy applications. The simulation is done on a laterally periodic domain. The domain extends for 3 km in the horizontal directions and 1 km vertically, and has a uniform grid resolution of 10 m. The microscale mean profiles of velocity and potential temperature are driven toward mesoscale mean profiles as computed by the Weather Research and Forecasting (WRF) numerical weather prediction tool through a profile assimilation technique (Allaerts et al., 2020). Such conditions are shown in Fig. 2. The code is executed with second-order accuracy in space and time. The time



step is chosen so that the Courant number does not exceed 0.75. A turbulence “spin-up” time is considered prior to the window of interest and ignored in the analysis. A differentiating aspect of this work is that the analysis is carried out on transient background conditions, driven by mesoscale mean quantities.

We note that the domain extent implicitly limits the maximum correlation and coherence distance, as well as the maximum integral length scale that the simulation is able to capture. However, investigations with larger domain sizes indicated that 3 km is well suited for flowfield observed during the period of interest.

4 Methodology & Results

4.1 Turbulence Spatial Correlation

The correlation coefficient, R_{ij} , between two points \mathbf{x} and $\mathbf{x} + \mathbf{r}$, where \mathbf{r} is a separation vector, is given by

$$R_{ij}(\mathbf{x}, \mathbf{r}, t) = \frac{\langle u_i(\mathbf{x} + \mathbf{r}, t) u_j(\mathbf{x}, t) \rangle}{\sqrt{\langle u_i^2(\mathbf{x} + \mathbf{r}, t) \rangle} \sqrt{\langle u_j^2(\mathbf{x}, t) \rangle}} \quad (1)$$

where u_i denotes the zero-mean turbulent fluctuations, and the angled brackets denote an ensemble average of realizations. Here we focus on autocorrelations, i.e. $i = j$. Throughout this work, we define $u = u_1$ as the streamwise, $v = u_2$ as the cross-stream, and $w = u_3$ as the vertical component of the flow. For clarity, when speaking of velocity components, we refer to “streamwise” and “cross-stream” components. However, when speaking of the directionality of separation vector, we refer to “along-wind” and “cross-wind” directions.

The idea is to perform two-point correlation computations with respect to a fixed point. We vary the second point so that the turbulence over a plane covering the computational domain is correlated with the fixed point. The result is a map of the correlation coefficients over this plane. This is useful in assessing how the turbulence evolves and allow us to obtain correlation coefficients between two points arbitrarily spaced. For a horizontal plane at a specific hub height (e.g., 80 m), we start by saving horizontal slices at 1 Hz from the LES for postprocessing. Picking the central point as the reference point ($\mathbf{r} = 0$), we expect (by definition) the correlation to be exactly 1 at this central point with an exponential decay with increasing \mathbf{r} . The domain size allows us to perform correlations with $|\mathbf{r}| \leq 1.5$ km.

The procedure is to apply Eq. (1) to all points on the plane with respect to a central point for each snapshot. Time averaging replaces ensemble averaging, but because the mesoscale conditions vary in time, a temporal average over the whole interval is not performed. Instead, shorter time averaging windows are used over which mesoscale conditions change relatively little. From a study on window size and overlap, we found that a 15-min window with 10-min overlap provided (i) enough data for smooth converged statistics, (ii) a short enough interval such that mean conditions did not change appreciably, and (iii) a large enough interval to accommodate large time-scale features. A goal of this analysis is to see how the correlation coefficients change with evolving conditions.

It is important to highlight the assumptions and limitations so far. In choosing the grid resolution, a bound on the smallest resolved scales is imposed, which for this type of numerical method is 4–5 times the grid resolution (Pope, 2001, p. 574). In



choosing a domain extent, a limit on the largest scales is also imposed. Domain sizes, though, are usually much larger than the
125 largest scales of interest. We assume horizontal homogeneity due to the periodic lateral boundaries.

4.2 Correlation Results

Performing the steps outlined above on the whole domain results in little realizations and noisy results. Keeping the largest
scales of interest in mind, and leveraging horizontal homogeneity, we split the domain into smaller subdomains and perform
local spatial correlation analysis. For this subdomain analysis, the correlation between each subdomain location and its central
130 point is established. Figure 3 shows the correlations for the three components of turbulence on a 3-by-3 grid of 1×1 km
subdomains. This strategy allows for more averaging and smoother statistics; however, it imposes a tighter limit on the largest
scales. The aforementioned temporal windowing imposes another limit on the largest time scale captured. The limit on the time
scale is not relevant for this problem, but it is worth mentioning.

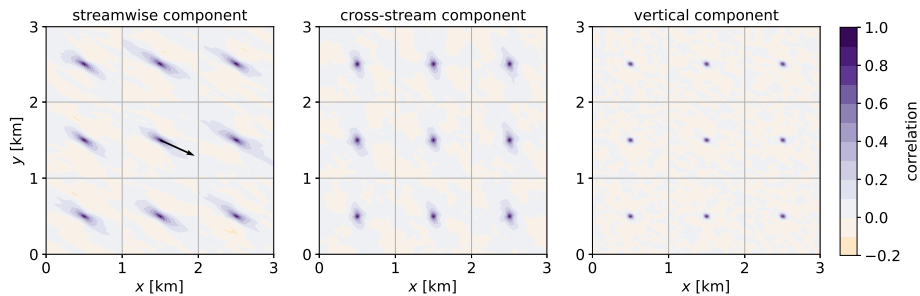


Figure 3. Contour plots of spatial correlation for the three turbulence components for the split-domain approach. Nine domains organized in a 3-by-3 grid are use. The goal is to have more realizations for an ensemble average. For each panel, an spatial average is shown in Fig.4. The black arrow indicates the mean direction of the wind.

The spatial average of the subdomains is shown next in Fig. 4. Note the axis limits and overall domain size after the ensemble
135 average. From this point forward, all results are related to the correlation analysis performed using the 3-by-3 grid of 1×1 km subdomains.

The results of this analysis show what is often intuitive by looking at typical boundary layer flow fields: the turbulent structure of the streamwise component of the turbulence is “stretched” in the along-wind direction, whereas structures formed by the other components are much more isotropic. The behavior of the streamwise component is much different in the cross-wind
140 versus the along-wind direction: within a relatively short distance, it becomes decorrelated and then slightly anticorrelated, meaning that one should expect alternating patterns of along-wind elongated structures containing streamwise velocity excesses arranged next to deficits. This spatio-temporal correlation analysis show similar results to that of Lukassen et al. (2018).

Because we compute autocorrelation maps for each overlapping time window within the analysis period, we can observe how turbulence autocorrelation varies as flow conditions change. Although the contour maps are very informative, we sought
145 ways to reduce the information they contain to quantities of interest that we can track versus time. As a first step, we sample

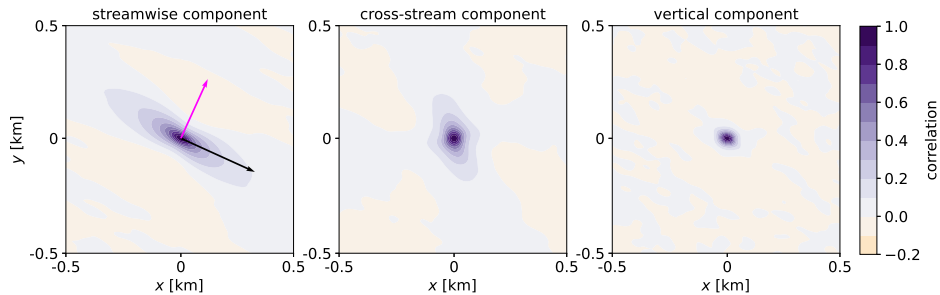


Figure 4. Contour plots of ensemble average of spatial correlation for the three turbulence components. The along- and cross-wind directions are indicated by the black and magenta arrows, respectively. The spatial correlation of the streamwise component is stretched in the direction of the wind (mostly from the Northwest, black arrow), while other components show no clear preferential direction.

autocorrelation coefficient values from the contour maps over along-wind- and cross-wind-oriented lines that pass through the central point (see black and magenta arrows in Fig. 4, which indicate the direction of these lines). The resulting plots of autocorrelation coefficient versus along-wind or cross-wind distance are shown in Fig. 5 for the streamwise component of the flow. In this figure, each light blue curve comes from the ensemble average at each time interval of 15 minutes. The red curve is the average of all the individual 15-min curves. The red curve is computed in order to establish a more direct comparison with observation data over the entire period of interest. By its definition in Eq. (1), the correlation coefficients are 1 at zero separation. The more gradual decay of correlation coefficient with along-wind versus cross-wind distance is clear. The autocorrelation of streamwise velocity fluctuation drops to effectively zero within 150 m in the cross-stream direction. However, in the along-wind direction, the correlation coefficient decay to zero is not fully captured over the half-length of the subdomain, even though the decorrelation length scale can be seen to be around 400–450 m for some of the time intervals.

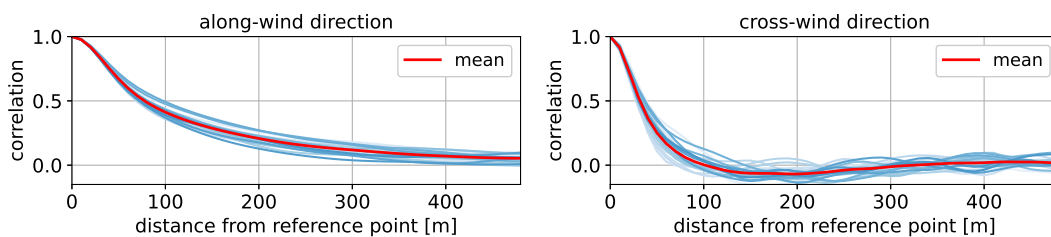


Figure 5. Correlation coefficients from Fig. 4 in the along- and cross-wind directions for the streamwise component. Each blue curve represents a 15-min interval, whereas the red curve is the mean over the time period of interest.

In the above spatial autocorrelation analysis, we examined spatial correlations where the separation vector is purely horizontal. The FINO1 data investigated come from a single meteorological mast that only contains vertical spacings between measurement points. To this end, we compute temporal autocorrelations of the observation data in order to compare the corre-

lations based on separations in different directions using a single field measurement point

$$160 \quad R_{ij}(\mathbf{x}, \tau) = \frac{\langle u_i(\mathbf{x}, t_0 + \tau) u_j(\mathbf{x}, t_0) \rangle}{\sqrt{\langle u_i^2(\mathbf{x}, t_0 + \tau) \rangle} \sqrt{\langle u_j^2(\mathbf{x}, t_0) \rangle}} \quad (2)$$

where τ is a separation in time. We transform between spatial separation and temporal separation in the along-wind direction by assuming the turbulence is frozen and advecting with the mean wind (Taylor, 1938).

To test the frozen turbulence assumption more definitively, we compute and compare the temporal correlation on the field and LES data. The results are shown in Fig. 6. Panel 6(a) shows temporal autocorrelations of the streamwise component of the velocity of the observed data, obtained at 80 m. In 6(a–c), each individual light-shade curve represents the correlations of a 15-min interval; whereas the dark shade curves are the average of the light curves, representing the average of the full 4-hour period of interest. Note that in panel 6(a), the individual curves are rather noisy. Therefore, to obtain some sort of ensemble average, we perform an average over the whole period. This average, indicated by the dark shade, can be compared with LES results. In panel 6(b), we show the temporal autocorrelations of the streamwise velocity components collected from nine virtual meteorological masts in the LES, so it is directly analogous to the observation results from panel 6(a). In panel 6(c), we show the correlation presented prior in Fig. 5 along the mean wind direction, converted to the time domain using Taylor’s hypothesis. Because of the spatial subdomain size and the mean advection speed, the maximum time separation computed is about 36 s. The reach of this curve is a direct result of splitting the domain. Finally, panel 6(d) shows the mean results (dark shade) of each panel 6(a–c) together for ease of comparison. Based on this exercise, noting the good match between the red and green curves, we conclude that frozen turbulence appears to be a reasonable assumptions and that it can be used to transform between spatial and temporal correlations. We note a mismatch between curves based on observed data versus LES in low values of time separation (from 0 to 10 s). This mismatch is possibly caused by the inability of the LES to resolve turbulence below its spatial and temporal filter scale.

The velocity spectra, Fig. 7, show the differences between the small-scale turbulence resolved by LES and that measured at the FINO1 for the first hour and the last hour of the period of interest. There is a good match between LES and observation data before the drop-off in resolved content by LES. The drop-off in energy for the LES occurs between 0.1 and 0.2 Hz, a result of its inability to capture such frequencies due to grid size limitations and mean wind speeds over the interval. The energy content of the LES is slightly higher than the content of the observation dataset for the last hour of the period at the low-frequency range, possibly a result of a delay of the LES turbulence to react to the slight ramp-down event that started at 04Z (Fig. 2(a), thus still exhibiting higher levels of TI (Fig. 2(c)). The velocity spectra are obtained using Welch’s algorithm with an overlapping (50%) 15-min Hamming window. No significant differences were observed by using a Hann window.

The integral length scale is obtained by integration of the spatial correlation curves presented in Fig. 5. The results are shown in Fig. 8(a), where integration is carried out until the correlation drops to 0.05. The same process is performed with the integral of the temporal autocorrelation curves to obtain the integral time scale. Again, we may use Taylor’s assumption to transform between the integral time and length scales, which was used to produce the (b) panel in Fig. 8. In canonical LES studies, stationary mesoscale conditions are usually the focus. Here, with mesoscale coupling and varying mesoscale conditions, we are able to study the effect of mesoscale transients on turbulence. In the conditions investigated in this work and as shown

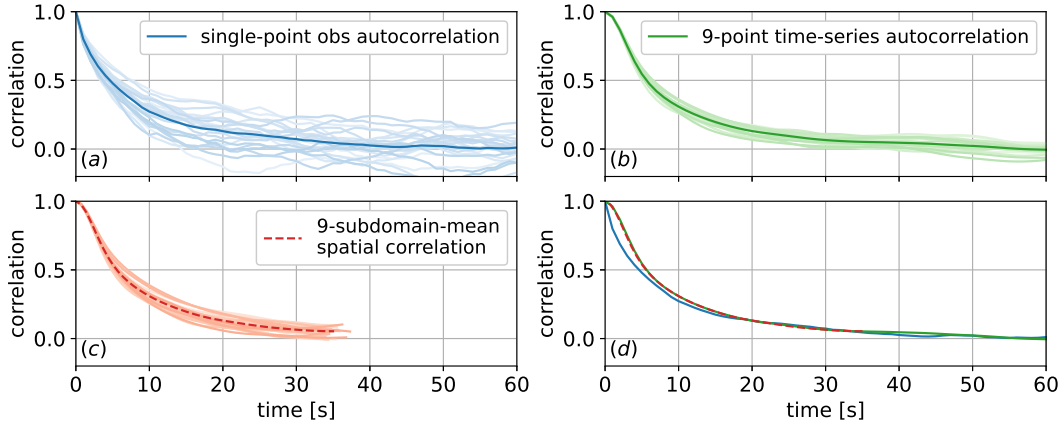


Figure 6. Comparison of spatial correlation and temporal autocorrelation of streamwise component of the velocity from LES with field data. Each lightly shaded curve represents one 15-min interval; the dark-shaded curve is the average of the light curves. (a) Temporal autocorrelation of single-mast observation data obtained at 80 m; (b) Temporal autocorrelation of 9 virtual meteorological masts from LES; (c) Spatial correlation results from LES transformed to time-domain; (d) Comparison of the mean curves of each panel.

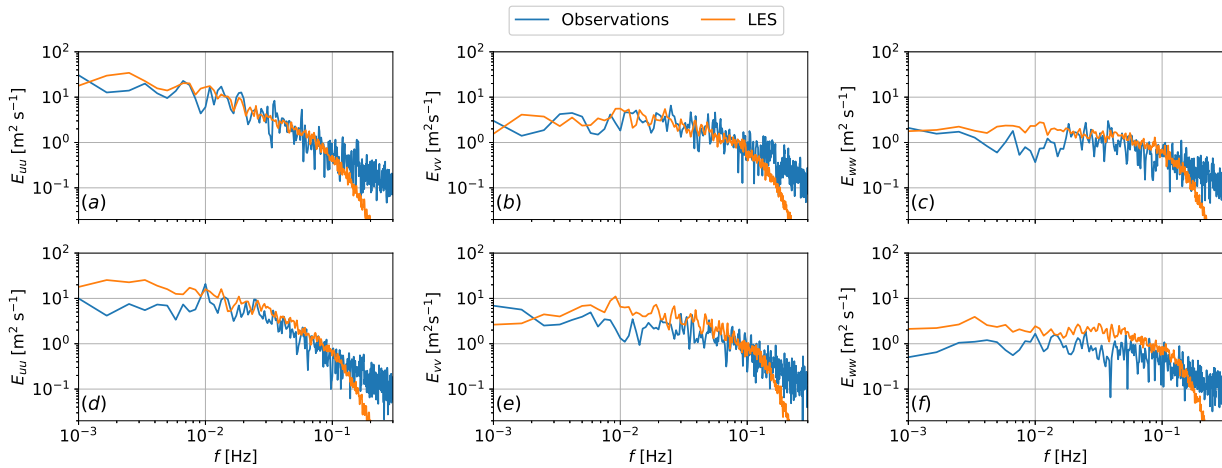


Figure 7. Comparison of power spectra of the three turbulence components (a,d) u , (b,e) v , and (c,f) w for the first hour (top row), and the last hour (bottom row) of the period of interest using 15-min Hamming windows.

in Fig. 8, the integral length scale can fluctuate from about 120 m to 150 m. In comparison, the integral length scale of the streamwise component in the cross-wind direction is about 3 to 4 times smaller than in the along-wind direction.

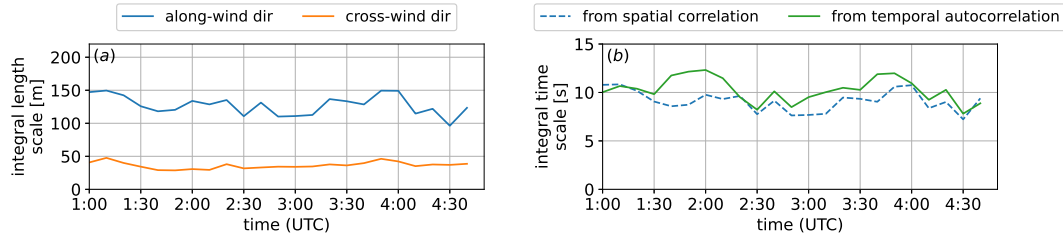


Figure 8. Integral scales variation of the 4-hour period of interest from LES. (a) Integral length scale of the streamwise component of the turbulence for the two directions; (b) Along-wind integral time scale calculated separately from spatial correlation and temporal autocorrelation data.

195 4.3 Turbulence Coherence over Arbitrary Separations

Knowing the integral length scales present in the flow, we compute a related but different statistic, coherence, with separation distances of the same order of magnitude. Here we focus on coherence magnitude, which we will simply refer to as “coherence.” It is the normalization of the magnitude of the cross spectra of velocity fluctuations. In other words, it describes the correlation between two time series as a function of frequency. The square of coherence magnitude between two signals i and j is defined as

$$\gamma_{ij}^2(f) = \frac{|S_{ij}(f)|^2}{S_{ii}(f) S_{jj}(f)} \quad (3)$$

where S_{ii} and S_{jj} are the power spectral density of signals i and j , and S_{ij} is the cross-power spectral density between i and j . The two signals are of individual components of the three-dimensional velocity vector $\mathcal{U} = (u, v, w)$ and are often given in terms of along-wind, cross-wind, or vertical separation distance δ . The type of coherence is given by the direction of the separation. For instance, the along-wind coherence of the streamwise component is given by $\gamma_{uu, \text{long}}^2$, where the two time series are of streamwise velocity at two locations separated by distance δ in the along-wind direction.

Coherence and correlation give similar information, but they differ in a few ways. Correlation shows how two quantities are related in physical space or time and can vary from -1 to $+1$. For example, if two sinusoidal signals are identical in amplitude and frequency, but have a phase lag at a certain separation distance, the correlation can lie anywhere between -1 and $+1$ depending on the phasing. For example, for a separation that aligns maxima with minima, the correlation will become anti-correlated with a value of -1 . On the other hand, coherence magnitude ranges from 0 to 1 and is not as sensitive to the phase lag because it uses cross-spectra magnitude. Two identical but phase lagged sinusoidal signals will have a coherence of 1 at only the frequency of the sine wave (the other frequencies would be undefined due to zero spectral information and the definition (3)). Although this work focuses on coherence magnitude, one can also examine the real and imaginary part of the coherence, which are termed “co-coherence” and “quad-coherence,” respectively, as outlined by Nybø et al. (2020). While coherence magnitude is a measure of the consistency of a phase relationship in the data, it does not have information on what



that phase relationship is – such information can be obtained by individual examination of co-coherence and quad-coherence separately.

The Kaimal exponential coherence model, suggested by the IEC standards, is only defined in the cross-wind and vertical
220 directions. An improvement to Davenport's, the model introduces an additional term that is a function of the separation distance, δ , and a coherence scale parameter, L_c . For the streamwise component of the velocity at two points, vertically or laterally separated by distance δ , with mean wind speed U , the coherence model reads

$$\gamma_{u u_{\text{lat,vert}}}^2(f, \delta) = \exp \left(-a \sqrt{\left(\frac{f \delta}{U} \right)^2 + \left(\frac{b \delta}{L_c} \right)^2} \right) \quad (4)$$

where a and b are tuning parameters. The IEC standards recommend $a = 12$ and $b = 0.12$. L_c is given as $8.1 \Lambda_1$, where Λ_1 is a
225 longitudinal scale parameter constant at 42 m for hub heights above 60 m.

Another common model for coherence adopted by the IEC guidelines is the Mann (1998) model. Both the Kaimal and Mann
models are based on spectral methods. While the Mann model is based more on physics and is a function of parameters used to
define the spectral tensor, the Kaimal model is based more on empirical formulations and less on physics, representing second-
order statistics. While they are computationally inexpensive and useful in the design process, they have two main limitations.
230 First, in some cases, when the flow field as computed by these models is used to drive load calculations, the results can be
different from one model to another (Eliassen and Obhrai, 2016), resulting in inconsistencies in load estimations. A second
limitation of the models is that atmospheric stability is not considered, as neutral stratification provided a sufficiently turbulent
condition at the time the models were developed.

To add longitudinal separation and to overcome the atmospheric stability limitation, studies have proposed more complex
235 models for longitudinal coherence. For example, adding longitudinal separation, Simley and Pao (2015) suggested

$$\gamma_{u u_{\text{long}}}^2(f, \delta) = \exp \left(- \left(a_1 \frac{\sigma}{U} + a_2 \right) \sqrt{\left(\frac{f \delta}{U} \right)^2 + \left(\frac{b_1 \delta}{L_c^{b_2}} \right)^2} \right) \quad (5)$$

where σ is the standard deviation of the wind speed, L_c is a measure of the integral length scale, and a_1 , a_2 , b_1 , and b_2 are
empirical constants adjusted using LES. In general, a number of exponential forms of the correlation decay have been proposed.
For more information, the interested reader should see the review by Martin et al. (2015)).

240 As mentioned, an accurate modeling of coherence is an important task. An increase in coherence has been shown to increase
the loads (Eliassen et al., 2015). Simulation tools for load estimation and thus design of wind turbines often follow IEC
standards, which suggest Eq. (4) for the streamwise velocity, thus neglecting the other components as well as the longitudinal
separations. Prior work focused on observation data has investigated other components in other separations (Saranyasontorn
et al., 2004).

245 Next, we show the estimation procedure for coherence and present some results. Due to the recognized inability of the current
setup to capture high-frequency phenomena, our focus will be at the low frequency range of $f < 0.15$ Hz, which corresponds
to about the rotational frequency of large offshore wind turbines.

4.4 Coherence Results

For vertically separated pairs of turbulence fluctuations, we sampled a vertical plane along the domain. For longitudinal and lateral separations, we use the same horizontal plane as the prior analysis. Interpolation is not needed for the vertically separated coherence, but it is needed within grid points for longitudinal and lateral separation. It is challenging to have grid points that are aligned with the wind direction because of the changing wind conditions.

The time series during the period of interest is not stationary, thus the spectra and subsequently the coherences are calculated using smaller intervals. The sample results shown in this section were obtained with 1 hour of data, using 50%-overlapping 15-min windows multiplied by the Hann function.

Figure 9 shows the curves obtained when focusing on the low-frequency range for the first hour of the interval of interest. There is no recommendation by the IEC standards for longitudinally separated points, so comparisons with the Simley and Pao (2015) model are presented for the streamwise velocity component, where it is defined.

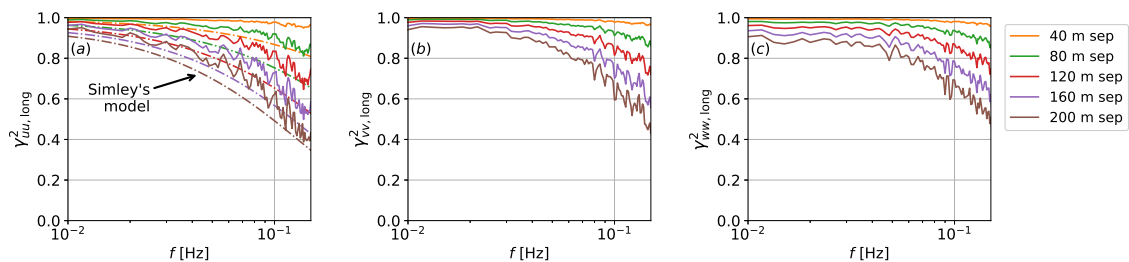


Figure 9. Coherence of the three turbulence components (a) u , (b) v , and (c) w separated longitudinally. Also shown are Simley’s model, Eq. (5). Note the logarithmic scale of the x -axis.

All three components show a high value of coherence at a relatively wide range of frequencies. The results match well the stability state correction proposed by Simley and Pao (2015). The results shown for the streamwise component of longitudinally separated points are also similar to those obtained using lidar data (Debnath et al., 2020), where for a case with about 140-m length scale, the drop-off occurred at around 0.1–0.2 Hz. No model is available for the other components.

Performing this analysis on longitudinal separation is relevant in the context of a wind farm, as one turbine might be in the wake of another upstream turbine. The flow description given by coherence curves may capture flow phase characteristics in the wake that can be relevant for load analysis of such waked turbines.

Coherence of the components of the turbulence separated laterally are shown in Fig. 10 for selected separation distances. Where Kaimal is defined, comparisons are provided. The IEC-recommended model overestimates the coherence in the frequency range investigated. The coherence values for laterally separated points (Fig. 10) are significantly lower than those encountered in longitudinally separated points (Fig. 9), suggesting that it may be important to properly account for the longitudinal separation, in addition to the lateral and vertical separations included in the IEC standard. While longitudinal separation can have an impact in a wind farm setting where multiple turbines are present, the lateral coherence may impact turbine loads,

especially as wind turbine rotors become larger. For lower lateral separation values, the coherence drops at very low frequencies. The results are consistent with those found by Bardal and Sætran (2016) where it was noted that given the same separation, lateral coherence is “significantly” smaller than longitudinal coherence. At higher frequencies, the computed curves do not drop to zero, which is result from numerical noise in the coherence calculations and thus unphysical (as similarly observed in Shaler et al. (2019)).

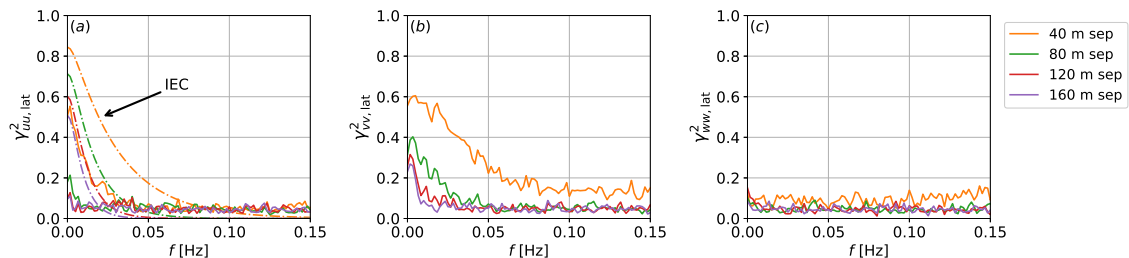


Figure 10. Coherence of the three turbulence components (a) u , (b) v , and (c) w separated laterally. Dash-dotted curves shown are obtained from the IEC-recommended Kaimal model, where defined.

The coherence for separations in the vertical direction is shown next in Fig. 11, with comparisons with Kaimal’s. In this case, separation is relative to a measurement point at a typical wind turbine hub height of 80 m. Negative separation means that one measurement point is below the reference point located at 80 m. The plots show a faster decay in the coherence of the streamwise component than in the other components, as well as a slight overprediction by Kaimal’s exponential coherence model. The vertical component decays the slowest with vertical separation. The results are consistent with prior investigations by Saranyasontorn et al. (2004) on much smaller separation distances. A small asymmetry between positive and negative separations is observed, and can be a result of the fact that the largest eddies present increase with height. Interestingly, for the vertical component, the negative separations result in stronger coherence decay with increasing frequency than that for the corresponding positive separations. The asymmetry effect appears to increase as the separation distance gets larger. We note that curves related to 20-m separation distance are showed for illustration and should not be deemed well-resolved as such separation includes only two LES grid points. Finally, the vertical coherence of v and w components do not approach 1 as the frequency tends to zero. This is caused by the fact that these components rarely include long-period fluctuations in the surface layer (Naito, 1983).

To assess if the LES results are within what one would expect, we compare two of the vertical separation curves to the observed data. The observation data were available at three heights, thus allowing two different separation distances with respect to the reference height of 80 m to be analyzed. Figure 12 shows the result. Note that prior comment about 20-m separation also applies here, as it constitutes only two LES grid points and thus results encompass a greater uncertainty. For the streamwise component, there is a good match, with the observation data following the LES much better than Kaimal’s model. The rather noisy nature of the observations curve is due to single-mast data. For the cross-stream and vertical components, the general trends and decay rate are also captured. We point out, nonetheless, that a model based on LES data could provide more

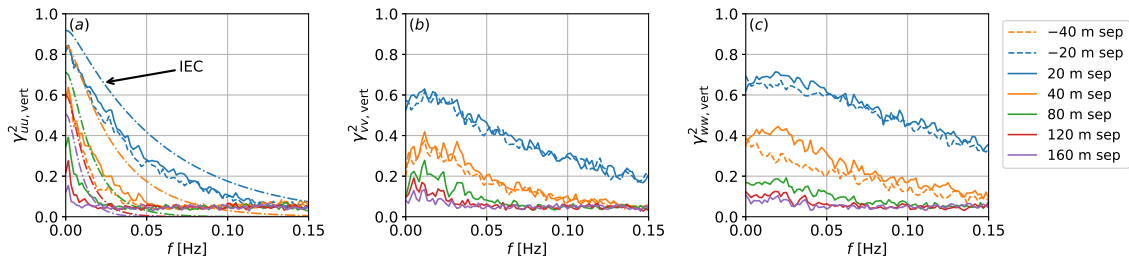


Figure 11. Coherence of the three turbulence components (a) u , (b) v , and (c) w separated vertically with respect to 80 m. Negative separation means that one of the points is below 80 m. Note the asymmetry shown by the same separation in different directions. Dash-dotted curves shown are obtained from the IEC-recommended Kaimal model, where defined.

information than no model. The present study suggests that, if considering vertical coherence over large separation distances, it might be important to consider the aforementioned asymmetry effect. With large separation distances, relevant for tall, large offshore wind turbines, the overall distance to the sea (or ground) level can lead to different characteristics in coherence (as shown in Fig. 11(c)). For example, the coherence between points at 40 m and 120 m above sea level is unlikely to be the same as the coherence between points located at 120 m and 200 m above sea level, even though they are separated by the same distance.

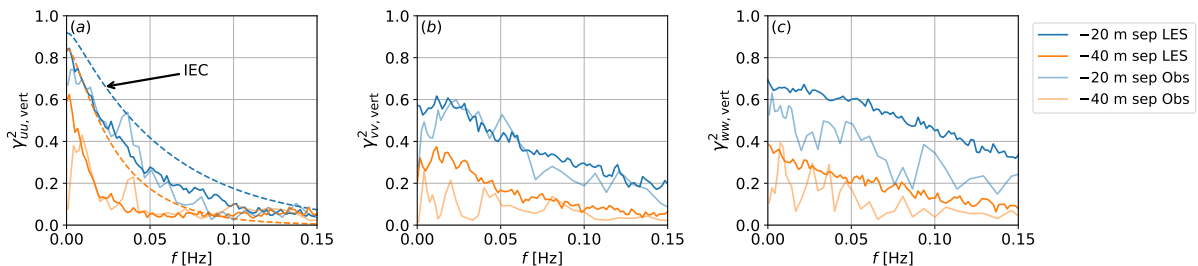


Figure 12. Comparison of coherence related to observed data for (a) u , (b) v , and (c) w components of the wind speed separated vertically with respect to 80 m. Negative separation means that one of the points is below 80 m. Dash-dotted curves shown are obtained from the IEC-recommended Kaimal model, where defined.

An advantage of using large-eddy simulation to obtain coherence is that we are able to perform the same analysis for an arbitrary separation distance. Some curves obtained at discrete separation values have been presented, but in Fig. 13 we show a contour plot of the same quantities for all separation distances. Although this figure also shows very small separations, we remind the reader that the values in such regions are not well resolved because the finest computational grid resolution is 10 m. The goal here is to point out an advantage of numerical models over field observations in that data can be sampled at virtually any location. Without that ability, we could not create the complete maps of coherence and correlations shown in Figs. 4 and 13.

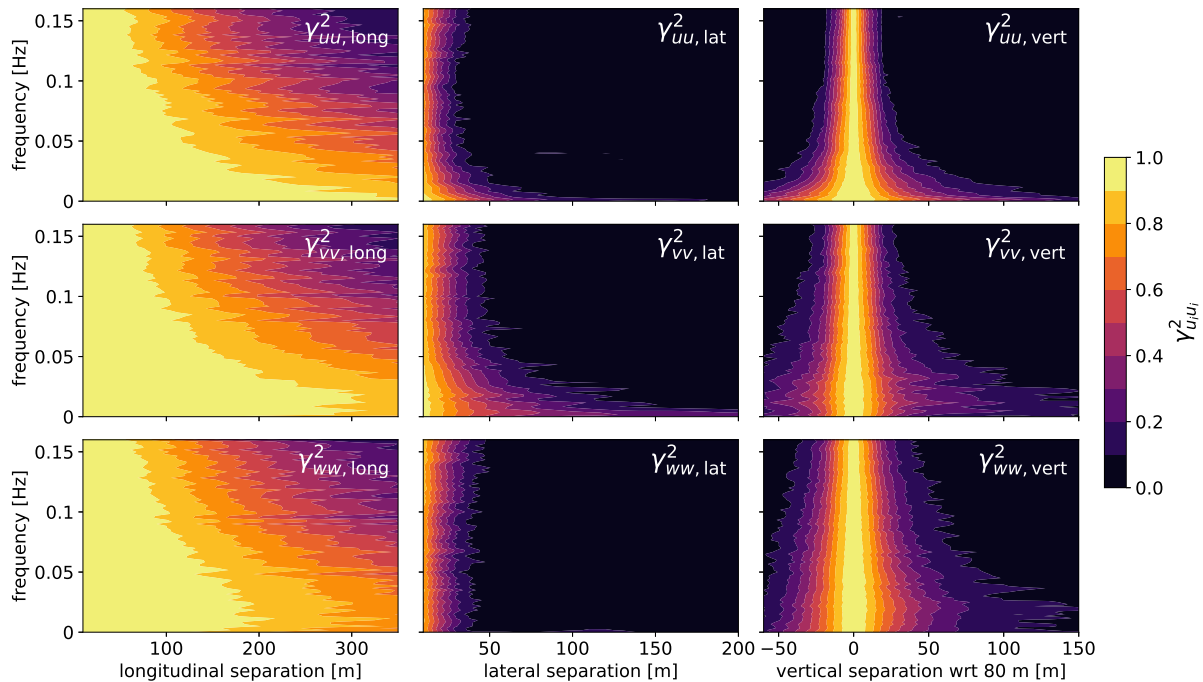


Figure 13. Contour of the coherence for all components of the turbulence, along all three separation directions, over a continuous range of separation distances. The diagonal panes are the component in the same direction of the separation.

310 Figure 13 summarizes the importance of modeling all three components of the turbulence. Perhaps not surprisingly, the highest coherence occurs for the component of turbulence in the same direction as the separation direction (diagonal panels). The coherence of large separation distances do not approach 1 as the frequency tends to zero, as reported in the literature (e.g. Doubrawa et al. (2019))

4.5 Cross Coherence

315 We calculate cross coherences uv , uw , and vw , each obtained from two distinct components of the turbulence at zero separation (same point). For the calculation of cross coherences shown here, we select points that lie on the 80 m above-ground-level plane and perform the computation. For each point, cross coherences are calculated and then an ensemble average is computed using all the individual cross coherences. The results for the first hour of the interval is are shown in Fig. 14.

320 Cross coherence is not usually considered in preliminary design and load analysis of new wind turbines. The isotropic von Karman model (Von Karman, 1948) considers all of them to be zero, due to the isotropy assumptions and lack of shear consideration. The Mann uniform shear model considers only uw coherence to be nonzero. This is what we observe in the cross coherence shown in Fig. 14. The largest cross coherence is found between the streamwise and vertical components, while no significant correlation exists between the streamwise and cross-stream turbulent components, and neither between the cross-

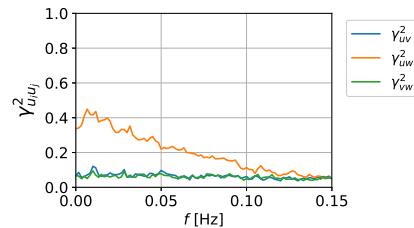


Figure 14. Mean cross coherence for points at the 80 m above-ground-level plane.

stream and vertical components (ignoring numerical noise). These findings are consistent with those from Saranyasootorn
325 et al. (2004) and the aforementioned study by Mann (1994). The uw coherence is related to the friction velocity and, therefore,
affected by the wind shear. This study adds to the study of Saranyasootorn et al. (2004) pointing out that it might be relevant
to account for the effect of uw -coherence when generating inflow with the goal of load analysis.

5 Discussion

The analysis procedure outlined in this study is general and can be applied to any LES solution of the atmospheric boundary
330 layer. The curves obtained through the analysis can then be used to inform a synthetic turbulence generator such as Turb-
Sim (Kelley and Jonkman, 2005). TurbSim has the option to generate synthetic inflow following the Kaimal model; options
which may be readily extended to use coherence characteristics obtained from a high-fidelity solution. Future work should
include a parametric study with varying atmospheric conditions, which will produce a set of coherence curves for each compo-
nent and separation direction. The additional curves can be used to further derive curves for intermediate conditions that
335 were not explicitly simulated. Ultimately, this would enable LES-informed time series of turbulence to be generated for any
condition. More accurate time-series of the turbulence can improve the representation of design load conditions that are used
on load estimations in lower fidelity wind turbine design codes. The ultimate impact is the ability to obtain less conservative
designs, relying less on simplified models like that of Kaimal et al. (1972), suggested by the current IEC standards.

The coherence magnitude is given by the cross-spectra normalized the auto spectra of the individual components of the
340 turbulence. The coupled effects of the difference components of the turbulence are expressed in the cross-spectra term. From
a statistical perspective, the information contained in the coherence fully defines two-point, second-order statistics of random
fields. Therefore, all the second-order dynamic properties are contained in these quantities and can be used to generate a field
that is consistent with those properties. We emphasize that these are the quantities that drive the dynamic response of a system
like a wind turbine rotor.

345 It is also important to note the grid spacing used in this work and the final applicability of such a model on modern large,
flexible rotors. The 10-m resolution limits the scale of the resolved turbulence and frequency of the computed coherence. For
instance, resolving turbulent structures at 20-m separation can be relevant near the tip of the blade and, at the current grid
spacing, 20-m separation results are not reliable. The general analysis applied to simulations with higher spatial resolution



would allow much more detailed investigations of the coherence in all three components, informing both how we model and
350 measure turbulence.

A higher spatial resolution would also push the cutoff frequency higher than the 0.15 Hz shown here and provide insight
into higher frequency, smaller scale turbulence. The procedure is also suitable for modeling turbine–turbine interactions in a
wind farm setting. For example, considering a row of turbines, one could process the data following the coherence analysis
presented here and come up with simple analytical models that could potentially include the wake of turbines within the
355 farm. Ultimately, such models can be used within other simulation tools for loads and fatigue (for example, OpenFAST and
FAST.Farm (Jonkman et al., 2017)).

Another interesting application of the analysis routine outlined is its use in the assessment of whether or not the turbulence
has reached a “developed” stage. Consider a wind farm simulation that has inflow without grid-scale resolved turbulence: a
fetch region in which both resolved and modeled quantities evolve would typically be observed. The length of this spatial region
360 is often determined by visual inspection of the flow field and, more quantitatively, using power spectral density. The correlation
analysis of streamwise and lateral flow presented here can be used as another metric to quantify when an equilibrium has been
reached and to help determine the fetch region extent.

6 Concluding Remarks

This work highlights the utility of computing turbulence correlations and coherence using turbulence-resolving LES data.
365 Coherence of the v and w components along all three directions do not appear to be negligible, even though the Kaimal
exponential coherence model—one of the models suggested by the IEC standards—ignores them. This work intends to highlight
that the process of creating coherent synthetic turbulence may be improved by knowledge gained through LES.

We showed that evolving conditions can change the way the flow is presented in terms of both integral scales and coherence
levels. For the period investigated, when the wind shear remained relatively constant with an exponent of 0.1–0.15, our analysis
370 indicates that frozen turbulence appears to be a suitable assumption when correlations are the main metric under investigation.
The coherence decay, however, is faster in some components and directions than others, suggesting that frozen turbulence may
not be applicable under other conditions. The variation of coherence decay among the different directions and components of
the wind speed can be significant. This is an important aspect of some flows that may be overlooked by simplified studies where
single-point first-order metrics (e.g., turbulent kinetic energy) are highlighted. A better understanding of the spatial structure
375 of the turbulence under different conditions can better inform turbulence models that are used for loads calculations. A higher
confidence in the estimations from such models could result in better estimate of a blade fatigue life.

This work demonstrates the wealth of additional information that can be gathered from a typical atmospheric LES, and
outlines the numerical limitations that need to be considered when using LES data. State-of-the-art atmospheric simulation
capabilities are continuing to evolve, and complex, large scenarios are now more routine practice. Some of these complex
380 scenarios include realistic weather conditions such as full diurnal cycles, frontal passages, low-level jets, among others. With
the rapid adoption of GPU-based LES codes, we are headed into ever faster, higher resolution workflows. Quantities such as



correlation, integral scales, coherence, and cross-spectral information are not often computed and discussed in typical atmospheric and wind plant studies. Here we demonstrate the additional insights that can be gained from site- and condition-specific studies, which could be further investigated and ultimately used to inform models.

385 *Code and data availability.* The LES code SOWFA is available at github.com/NREL/SOWFA-6. Input files for the case analyzed in this work are available at github.com/a2e-mmc/SOWFA-setups/tree/master/offshore_FINO1_intCoupled. Output data are available upon request.

Author contributions. This work was led by RT, who performed the simulations and carried out the analysis. RT and MC formulated the research goals and aim of the study. MC, EQ, and PV supervised the conceptualization, and contributed to discussions on the formal analysis. RT prepared the manuscript with contributions and review from all co-authors.

390 *Competing interests.* One of the co-authors is a member of the editorial board of Wind Energy Science.

Acknowledgements. This work was authored by the National Renewable Energy Laboratory, operated by Alliance for Sustainable Energy, LLC, for the U.S. Department of Energy (DOE) under Contract No. DE-AC36-08GO28308. Funding provided by the U.S. Department of Energy Office of Energy Efficiency and Renewable Energy Wind Energy Technologies Office. This research was performed using computational resources sponsored by the Department of Energy's Office of Energy Efficiency and Renewable Energy and located at the National
395 Renewable Energy Laboratory. The views expressed in the article do not necessarily represent the views of the DOE or the U.S. Government. The U.S. Government retains and the publisher, by accepting the article for publication, acknowledges that the U.S. Government retains a nonexclusive, paid-up, irrevocable, worldwide license to publish or reproduce the published form of this work, or allow others to do so, for U.S. Government purposes. The authors thank Patrick Hawbecker from NCAR for providing the mesoscale dataset used in this work. FINO1 data made freely available by the Bundesamt für Seeschifffahrt und Hydrographie (BSH) agency is greatly appreciated.



400 References

- Allaerts, D., Quon, E., Draxl, C., and Churchfield, M.: Development of a Time-Height Profile Assimilation Technique for Large-Eddy Simulation, *Boundary-Layer Meteorology*, 176, 329–348, 2020.
- Andersen, O. J. and Løvseth, J.: The Frøya database and maritime boundary layer wind description, *Marine Structures*, 19, 173–192, 2006.
- Bardal, L. and Sætran, L.: Spatial correlation of atmospheric wind at scales relevant for large scale wind turbines, in: *Journal of Physics: Conference Series*, vol. 753, p. 032033, IOP Publishing, 2016.
- 405 Berg, J., Natarajan, A., Mann, J., and Patton, E. G.: Gaussian vs non-Gaussian turbulence: impact on wind turbine loads, *Wind Energy*, 19, 1975–1989, 2016.
- Cheyne, E., Jakobsen, J. B., and Obhrai, C.: Spectral characteristics of surface-layer turbulence in the North Sea, *Energy Procedia*, 137, 414–427, 2017.
- 410 Churchfield, M. J., Lee, S., Michalakes, J., and Moriarty, P. J.: A numerical study of the effects of atmospheric and wake turbulence on wind turbine dynamics, *Journal of Turbulence*, 13, 1–32, <https://doi.org/10.1080/14685248.2012.668191>, 2012.
- Davenport, A. G.: The application of statistical concepts to the wind loading of structures., *Proceedings of the Institution of Civil Engineers*, 19, 449–472, 1961.
- Debnath, M., Brugger, P., Simley, E., Doubrawa, P., Hamilton, N., Scholbrock, A., Jager, D., Murphy, M., Roadman, J., Lundquist, J. K.,
415 et al.: Longitudinal coherence and short-term wind speed prediction based on a nacelle-mounted Doppler lidar, in: *Journal of Physics: Conference Series*, vol. 1618, p. 032051, IOP Publishing, 2020.
- Doubrawa, P., Churchfield, M. J., Godvik, M., and Sirmivas, S.: Load response of a floating wind turbine to turbulent atmospheric flow, *Applied Energy*, 242, 1588–1599, 2019.
- Eidsvik, K. J.: Large-sample estimates of wind fluctuations over the ocean, *Boundary-layer meteorology*, 32, 103–132, 1985.
- 420 Eliassen, L. and Obhrai, C.: Coherence of turbulent wind under neutral wind conditions at FINO1, *Energy Procedia*, 94, 388–398, 2016.
- Eliassen, L., Jakobsen, J., and Krokstad, J.: The effect of turbulent wind field on loads of a wind turbine rotor of increasing size, in: *14th International Conference on Wind Engineering*, Porto Alegre, Brazil, 2015.
- Holtslag, M., Bierbooms, W., and Van Bussel, G.: Wind turbine fatigue loads as a function of atmospheric conditions offshore, *Wind Energy*, 19, 1917–1932, 2016.
- 425 IEC 61400-1: Wind energy generation systems – Part 1: Design requirements, Edition 4.0, International Electrotechnical Commission, 2019.
- Jonkman, J. M., Annoni, J., Hayman, G., Jonkman, B., and Purkayastha, A.: Development of FAST.Farm: A new multi-physics engineering tool for wind-farm design and analysis, in: *35th Wind Energy Symposium*, p. 0454, 2017.
- Kaimal, J. C., Wyngaard, J. C., Izumi, Y., and Coté, O. R.: Spectral characteristics of surface-layer turbulence, *Quarterly Journal of the Royal Meteorological Society*, 98, 563–589, 1972.
- 430 Kelley, N.: Turbulence-turbine interaction: The basis for the development of the TurbSim stochastic simulator, *Contract*, 303, 275–300, 2011.
- Kelley, N. D. and Jonkman, B. J.: Overview of the TurbSim stochastic inflow turbulence simulator, Tech. rep., National Renewable Energy Lab.(NREL), Golden, CO (United States), 2005.
- Kelley, N. D., Jonkman, B. J., Scott, G., Bialasiewicz, J., and Redmond, L. S.: Impact of coherent turbulence on wind turbine aeroelastic response and its simulation, Tech. rep., National Renewable Energy Lab.(NREL), Golden, CO (United States), 2005.
- 435 Li, F., Zou, L., Song, J., Liang, S., and Chen, Y.: Investigation of the spatial coherence function of wind loads on lattice frame structures, *Journal of Wind Engineering and Industrial Aerodynamics*, 215, 104675, 2021.



- Lukassen, L. J., Stevens, R. J., Meneveau, C., and Wilczek, M.: Modeling space-time correlations of velocity fluctuations in wind farms, *Wind energy*, 21, 474–487, 2018.
- Mann, J.: The spatial structure of neutral atmospheric surface-layer turbulence, *Journal of fluid mechanics*, 273, 141–168, 1994.
- 440 Mann, J.: Wind field simulation, *Probabilistic engineering mechanics*, 13, 269–282, 1998.
- Martin, C. M. S., Lundquist, J. K., and Handschy, M. A.: Variability of interconnected wind plants: correlation length and its dependence on variability time scale, *Environmental Research Letters*, 10, 044 004, 2015.
- Naito, G.: Spatial structure of surface wind over the ocean, *Journal of Wind Engineering and Industrial Aerodynamics*, 13, 67–76, 1983.
- Nybø, A., Nielsen, F. G., Reuder, J., Churchfield, M. J., and Godvik, M.: Evaluation of different wind fields for the investigation of the
445 dynamic response of offshore wind turbines, *Wind Energy*, 23, 1810–1830, 2020.
- Pope, S. B.: *Turbulent flows*, 2001.
- Robertson, A., Sethuraman, L., Jonkman, J. M., and Quick, J.: Assessment of Wind Parameter Sensitivity on Extreme and Fatigue Wind Turbine Loads, in: *AIAA Scitech 2018 Forum*, 2018.
- Saranyasootorn, K., Manuel, L., and Veers, P. S.: A comparison of standard coherence models for inflow turbulence with estimates from
450 field measurements, *J. Sol. Energy Eng.*, 126, 1069–1082, 2004.
- Sathe, A. and Bierbooms, W.: Influence of different wind profiles due to varying atmospheric stability on the fatigue life of wind turbines, in: *Journal of Physics: Conference Series*, vol. 75, p. 012056, IOP Publishing, 2007.
- Sathe, A., Mann, J., Barlas, T., Bierbooms, W., and Van Bussel, G.: Influence of atmospheric stability on wind turbine loads, *Wind Energy*, 16, 1013–1032, 2013.
- 455 Shaler, K., Jonkman, J., Doubrava Moreira, P., and Hamilton, N.: FAST.Farm response to varying wind inflow techniques, Tech. rep., National Renewable Energy Lab.(NREL), Golden, CO (United States), 2019.
- Simley, E. and Pao, L. Y.: A longitudinal spatial coherence model for wind evolution based on large-eddy simulation, in: *2015 American Control Conference (ACC)*, pp. 3708–3714, IEEE, 2015.
- Taylor, G. I.: The spectrum of turbulence, in: *Proceedings of the Royal Society of London A: Mathematical, Physical and Engineering Sciences*, vol. 164, pp. 476–490, The Royal Society, 1938.
- 460 Thresher, R., Holley, W., Smith, C., Jafarey, N., and Lin, S.: Modeling the response of wind turbines to atmospheric turbulence, Tech. rep., Oregon State Univ., Corvallis (USA). Dept. of Mechanical Engineering, 1981.
- Veers, P., Dykes, K., Lantz, E., Barth, S., Bottasso, C. L., Carlson, O., Clifton, A., Green, J., Green, P., Holttinen, H., et al.: Grand challenges in the science of wind energy, *Science*, 366, eaau2027, 2019.
- 465 Von Karman, T.: Progress in the statistical theory of turbulence, *Proceedings of the National Academy of Sciences of the United States of America*, 34, 530, 1948.